

Radio Emission with Dust: A Bow-shock Interpretation for the TDE Candidate AT 2019avd

Downloaded from: https://research.chalmers.se, 2026-11-27 07:44 UTC

Citation for the original published paper (version of record):
Wei, S., Wang, Y., Mou, G. et al (2026). Radio Emission with Dust: A Bow-shock Interpretation for the TDE Candidate AT 2019avd. Astrophysical Journal, 1010(1).
http://dx.doi.org/10.3847/1538-4357/aea4a8

N.B. When citing this work, cite the original published paper.

research.chalmers.se offers the possibility of retrieving research publications produced at Chalmers University of Technology. It covers all kind of research output: articles, dissertations, conference papers, reports etc. since 2004. research.chalmers.se is administrated and maintained by Chalmers Library

(article starts on next page)

The Astrophysical Journal, 1010:52 (16pp), 2026 October 10 https://doi.org/10.3847/1538-4357/aea4a8
© 2026. The Author(s). Published by the American Astronomical Society.
OPEN ACCESS

Radio Emission with Dust: A Bow-shock Interpretation for the TDE Candidate AT 2019avd

Shuyuan Wei[1], Yanan Wang[2], Guobin Mou[3], Linhui Wu[4], Santiago del Palacio[5], Ranieri D. Baldi[6], Xiaolong Yang[4], and Yang Huang[1,2]
[1] School of Astronomy and Space Sciences, University of Chinese Academy of Sciences, Beijing 100049, People's Republic of China
[2] National Astronomical Observatories, Chinese Academy of Sciences, 20A Datun Road, Beijing 100101, People's Republic of China; wangyn@bao.ac.cn
[3] Department of Physics and Institute of Theoretical Physics, Nanjing Normal University, Nanjing 210023, People's Republic of China; gbmou@njnu.edu.cn
[4] Shanghai Astronomical Observatory, Chinese Academy of Sciences, 80 Nandan Road, Shanghai 200030, People's Republic of China
[5] Department of Space, Earth and Environment, Chalmers University of Technology, SE-412 96 Gothenburg, Sweden
[6] INAF—Istituto di Radioastronomia, Via P. Gobetti 101, I-40129 Bologna, Italy
Received 2026 February 14; revised 2026 September 1; accepted 2026 September 7; published 2026 October 7

Abstract

Forward shocks produced by interactions between a single ejected blob and the circumnuclear medium (CNM) around a supermassive black hole are widely invoked to explain radio emission from tidal disruption events (TDEs). However, recent observational evidence such as rapidly rising radio emission, double-peaked broadband spectral energy distributions, and declining shock energies at late times poses challenges to this picture. Alternative scenarios have therefore been proposed, including bow shocks arising from outflows colliding with dense clouds, the production of new ejecta at late times, and variations in microphysical parameters. To investigate the roles of these factors, we analyze the long-lived radio flare of the TDE candidate AT 2019avd, for which dust has been identified through mid-infrared observations, using a radio dataset spanning more than 5 yr. We find that a bow-shock scenario can account for the majority of the observed radio emission, while a forward shock, or an additional bow shock involving different clouds, may begin to dominate at late times. However, a forward-shock scenario remains viable when allowing for evolving microphysical parameters and more complex CNM structures. We discuss the remaining tensions in both the outflow–CNM and outflow–cloud interaction scenarios.

Unified Astronomy Thesaurus concepts: High energy astrophysics (739); Supermassive black holes (1663); Radio transient sources (2008); Radio continuum emission (1340)

1. Introduction

Tidal disruption events (TDEs) are nuclear transients that occur when a star is tidally shredded upon passing too close to a supermassive black hole (SMBH; J. G. Hills 1975; M. J. Rees 1988). Their emission can temporarily illuminate dormant SMBHs and the unresolved nuclear regions of distant galaxies on subparsec scales. Characterizing the circumnuclear medium (CNM), including gas and dust, requires indirect diagnostic methods. For example, extreme coronal-line emitters probe the properties of circumnuclear gas around SMBHs (e.g., M. Newsome et al. 2024), while mid-infrared (IR) emission traces the reverberation radii of dust heated by optical to soft X-ray flares from TDEs (e.g., N. Jiang et al. 2016; W. Lu et al. 2016; S. van Velzen et al. 2016). Radio emission in TDEs is generally attributed to synchrotron radiation from external shocks produced as a TDE-driven outflow or jet interacts with the CNM (see K. D. Alexander et al. 2020 for a review). ASASSN-14li (D. R. Pasham & S. van Velzen 2018) and AT 2020afhd (Y. Wang et al. 2025) are two reported exceptions, with their radio emission instead linked directly to jet activity through strong X-ray–radio correlations. In contrast to observations at other wavelengths, which primarily probe radiative energy output, radio observations uniquely constrain the properties of the ejected material.

Original content from this work may be used under the terms of the Creative Commons Attribution 4.0 licence. Any further distribution of this work must maintain attribution to the author(s) and the title of the work, journal citation and DOI.

Radio TDEs exhibit a wide range of radio luminosities, spanning from 10^{37} to 10^{42} erg s^{-1}, with substantial diversity in their durations, onset times, evolution of the spectral energy distribution (SED; K. D. Alexander et al. 2020), and short-term variability (Y. Wang et al. 2025). To date, four events with luminous radio emission, $\nu L_\nu \gtrsim 10^{40}$ erg s^{-1}, have been attributed to on-axis relativistic jets, i.e., Swift J1644+57 (J. S. Bloom et al. 2011; B. A. Zauderer et al. 2011; E. Berger et al. 2012; T. Eftekhari et al. 2018), Swift J2058+05 (S. B. Cenko et al. 2012), Swift J1112.2-8238 (G. C. Brown et al. 2015), and AT2022cmc (I. Andreoni et al. 2022; D. R. Pasham et al. 2023; L. Rhodes et al. 2023). By contrast, many optically discovered TDEs exhibit substantially fainter radio emission, with $\nu L_\nu \lesssim 10^{39}$ erg s^{-1}. The physical mechanisms powering this population remain uncertain. Proposed scenarios include off-axis jets (e.g., AT 2018hyz; Y. Cendes et al. 2022; T. Matsumoto & T. Piran 2023; I. Sfaradi et al. 2024), internal shocks within jets (e.g., ASASSN-14li; D. R. Pasham & S. van Velzen 2018), nonrelativistic winds (e.g., AT 2019dsg; Y. Cendes et al. 2021; AT 2020opy; A. J. Goodwin et al. 2023b; AT 2020zso; C. T. Christy et al. 2026; AT 2024tvd; I. Sfaradi et al. 2025), collision-induced outflows (e.g., AT 2019azh; A. J. Goodwin et al. 2022; AT 2020vwl; A. J. Goodwin et al. 2023a), and unbound tidal debris streams (theoretically; J. Krolik et al. 2016; A. Yalinewich et al. 2019; and as an alternative for AT 2020vwl; A. J. Goodwin et al. 2023a).

While most models invoke a forward shock produced as an outflow propagates into the hot, diffuse CNM (K. D. Alexander

et al. 2020), bow shocks generated by interactions between the outflow and dense clouds have also been proposed as an alternative (G. Mou & W. Wang 2021; G. Mou et al. 2022). The main distinction between these scenarios lies in the physical interpretation of the radio-inferred parameters. In the forward-shock picture, the inferred radius corresponds to the location of the expanding shock front, and the inferred density represents the CNM density at that radius, enabling constraints on the radial density profile under assumptions about the outflow geometry and microphysics. In the bow-shock picture, by contrast, the radio emission originates from shocks wrapping around dense clouds. The inferred quantities then characterize the bow-shock properties themselves: the inferred radius corresponds to their characteristic scale, which is expected to be comparable to the cloud radius, whereas the inferred density traces that of the incident outflow rather than the ambient CNM. This latter scenario has been proposed to explain the delayed and rapidly rising radio emission of AT 2018cqh, and hydrodynamic calculations have shown that it can reproduce the observed radio evolution (L. Yang et al. 2025). Additional observations also suggest that a single-component forward-shock model may not always provide a complete description. For example, the transient double-peaked radio SED of AT 2020zso provides evidence for multiple physically distinct outflow components, while the interpretation of the late-time radio evolution of AT 2021sdu is complicated by possible host-galaxy contamination (C. T. Christy et al. 2026). More complex outflow structures, multiple ejecta episodes, environmental inhomogeneities, or evolving microphysical parameters may therefore be required in some events. Identifying the physical origin and geometry of the radio-emitting shocks is essential for a robust interpretation of the inferred outflow and CNM properties.

AT 2019avd is a nuclear transient characterized by two consecutive flaring episodes in the optical and IR bands (A. Malyali et al. 2021; Y. Wang et al. 2023). A growing number of studies have shown that TDEs can exhibit optical rebrightening (Y. Yao et al. 2023). In AT 2019avd, the X-ray decline lagged the optical and UV fading by approximately 80 days, in contrast to the behavior commonly observed in AGN. A. Malyali et al. (2021) also reported Bowen fluorescence features and high-ionization coronal lines in the optical spectra of AT 2019avd. Radio emission coincident with the second optical flare and the X-ray brightening was subsequently detected (Y. Wang et al. 2023). Very Large Array (VLA) and Very Long Baseline Array (VLBA) observations revealed the emergence of a compact radio source with a nonthermal spectrum, interpreted as emission from an evolving ejecta component associated with a change in the black hole accretion state (Y. Wang et al. 2023). A. J. Goodwin et al. (2025) further showed that the inferred outflow properties of AT 2019avd are broadly consistent with those of other radio TDEs. Taken together, these properties favor a TDE interpretation, although the possibility that AT 2019avd represents a new class of nuclear transient cannot yet be excluded.

The mid-IR emission from AT 2019avd is consistent with a dust echo from material located at a distance of approximately 0.03 pc from the SMBH. The long-lived radio emission, together with the presence of circumnuclear dust, makes AT 2019avd an ideal laboratory for probing the temporal evolution of outflows, distinguishing their physical origins, and assessing the relative roles of forward shocks and bow shocks.

In this work, we present a comprehensive analysis of the radio properties of AT 2019avd, utilizing data collected over 5 yr. The paper is structured as follows. Section 2 describes the radio observations and data reduction; Section 3 presents the multiepoch spectral fits, and tests (i) an outflow–CNM forward-shock interpretation using analytical prescriptions and (ii) an outflow–cloud bow-shock interpretation using hydrodynamical simulations; Section 4 discusses the outflow origin under outflow–CNM scenario and potential tensions with both the outflow–CNM and outflow–cloud scenarios; and Section 5 summarizes our conclusions.

2. Observations and Data Reduction

We present the observation log for AT 2019avd in Table A1. The log incorporates data from Y. Wang et al. (2023), which reports some VLA and VLBA flux measurements, as well as our own observational dataset.

In this work, uncertainties and upper/lower limits are quoted at the 1σ and 3σ confidence levels, respectively. We adopt a redshift of 0.028 from the Transient Name Server,[7] corresponding to a luminosity distance of $D = 130$ Mpc (Y. Wang et al. 2023). The black hole mass is taken to be $M_{\rm BH} = 10^{6.3}\,M_{\odot}$ from A. Malyali et al. (2021).

2.1. VLA

We obtained three radio observations of AT 2019avd with the VLA (program IDs: 23B-301 and 24A-434; PI: Y. Wang). These observations cover the *L*, *S*, *C*, *X*, and *K* bands (see more details in Table A1).

The data were reduced in the Common Astronomy Software Applications package (CASA v6.6.6; CASA Team et al. 2022). We applied the VLA CASA calibration pipeline (v2025.1.0.32) for standard calibration and automated flagging, followed by automated self-calibration using the VLA imaging pipeline task HIF_SELFCAL. Calibrated visibilities were imaged with TCLEAN into continuum images in frequency bins, using AUTO-MULTITHRESH to guide deconvolution. The resulting images typically reach a residual rms of $\sim$100 μJy beam^{-1}.

Unless explicitly mentioned, flux densities were measured by fitting a single Gaussian at the position of AT 2019avd in the cleaned images using IMFIT. For measurements obtained with all facilities, the uncertainties were computed by adding the statistical error in quadrature with a 5% systematic term to account for the absolute flux scale.

2.2. ATCA

We conducted four epochs of observations of AT 2019avd using the Australia Telescope Compact Array (ATCA) as part of programs C3615, C3662, and C3755 (PI: Y. Wang). Each epoch included observations in the *C*/*X*-band centered at 5.5 GHz and 9 GHz (with a 2 GHz bandwidth per window) and in the *L*-band centered at 2.1 GHz (with a 2 GHz bandwidth). For all ATCA observations, 0823−500 was used as the flux and bandpass calibrator, and 0823+033 as the phase calibrator.

The data were reduced in CASA following standard procedures, and images were produced using the task TCLEAN.

[7] https://www.wis-tns.org/object/2019avd

In the L band, significant sidelobe contamination from nearby bright sources was identified. To improve the dynamic range, we performed two rounds of phase-only self-calibration on the L-band target visibilities.

In the C-band observation of epoch 9, the relatively large synthesized beam resulted in mild blending with a nearby source. We therefore employed two CLEAN masks, i.e., one centered on AT 2019avd and one on the nearby source, during deconvolution, and adopted the integrated flux density measured from the TCLEAN CLEAN-component `model` image within an aperture matched to the restoring beam and centered on the position of AT 2019avd. The corresponding statistical uncertainty was taken to be the local rms noise measured in a nearby source-free region of the corresponding restored image.

2.3. VLASS

We analyzed the Karl G. Jansky Very Large Array Sky Survey (VLASS; M. Lacy et al. 2020) epoch 3 data covering the position of AT 2019avd using the user-defined VLASS imaging scripts (E. Carlson et al. 2022). We first applied the VLASS Single-Epoch Imaging Pipeline (SEIP) to perform phase-only self-calibration on the standard pipeline-calibrated measurement sets. To constrain the spectral properties of the source, we subsequently ran the Coarse-Cube Imaging Pipeline (CCIP), producing images in two spectral subbands centered at 2.5 and 3.5 GHz, each with a bandwidth of 1 GHz.

The flux densities for each epoch are listed in Table A1. The target remained unresolved throughout our observations.

3. Results

To place the radio evolution of AT 2019avd in the context of other radio-detected TDEs, Figure 1 compares its 5 GHz luminosity with those of a selected sample. AT 2019avd exhibits a delayed rise, reaches its peak radio luminosity at 1445 days after discovery, and subsequently fades rapidly. Its radio luminosity remains substantially below those of the canonical on-axis jetted TDEs.

3.1. Spectral Fitting

We fitted the radio SED at each epoch using the synchrotron self-absorbed (SSA) spectrum described by J. Granot & R. Sari (2002), adopting the spectral regime $\nu_{\rm m} < \nu_{\rm a} < \nu_{\rm c}$ (where $\nu_{\rm m}$ is the synchrotron frequency corresponding to the minimum electron Lorentz factor, $\nu_{\rm a}$ is the SSA frequency, and $\nu_{\rm c}$ is the synchrotron cooling frequency):

$$F(\nu) = F_{\rm norm} \times \left(\frac{\nu}{5\ {\rm GHz}}\right)^{b_2} \times \left[1 + \left(\frac{\nu}{\nu_a}\right)^{s_2(b_2-b_3)}\right]^{-\frac{1}{s_2}}. \quad (1)$$

Here, $F_{\rm norm}$ is the normalization flux density, and p is the electron energy index for a power-law distribution $N(\gamma_{\rm e}) \propto \gamma_{\rm e}^{-p}$ ($\gamma_{\rm e} \geqslant \gamma_{\rm m}$, where $\gamma_{\rm m}$ is the minimum Lorentz factor). The spectral slopes are fixed as $b_2 = 2.5$ (SSA slope) and $b_3 = \frac{1-p}{2}$ (optically thin slope), with the break smoothness parameter given by $s_2 = 1.47 - 0.21p$.

We performed Bayesian inference using `bilby` (G. Ashton et al. 2019; C. Talbot et al. 2025) with the `dynesty` sampler (J. S. Speagle 2020; S. Koposov et al. 2025), employing 1000 live points and terminating the sampling when the estimated remaining log-evidence satisfied $\Delta \ln \mathcal{Z} < 0.1$. We adopted uniform priors of $\nu_{\rm a} \in [0.1,\ 9.0]$ GHz and $F_{\rm norm} \in [10^1,\ 10^6]\ \mu$Jy. Given the limited high-frequency sampling ($\nu \gg \nu_{\rm a}$) in the early epochs, the electron energy index p is poorly constrained and highly degenerate with the break-smoothness parameter. We therefore used epoch 4, which has the broadest frequency coverage, to constrain p. For this epoch we adopted a uniform prior of $p \in [2.0, 4.0]$ and obtained $p = 2.91 \pm 0.10$. We then fix $p = 2.91$ in the SED modeling for all epochs.

The multiepoch radio spectra are well fit by the SSA model, with the resulting fits shown in Figure 2. From the posterior samples, we derived the observed peak frequency $\nu_{\rm p}$ and peak flux density $F_{\rm p}$ for each epoch. The spectral peak is not directly detected in the last two epochs. We therefore adopt conservative one-sided constraints, taking $F_{\rm p} > F_i$, where F_i is the brightest observed flux density, and $\nu_{\rm p} < \nu_{i+1}$, where ν_{i+1} is the frequency of the next higher-frequency data point. To characterize the temporal evolution of $\nu_{\rm p}$ and $F_{\rm p}$, we fitted both curves with power-law models and found that epoch 1 significantly deviates from the fits to the other epochs. The best-fitting parameters are indicated in Figure 3. While $\nu_{\rm p}$ exhibits a monotonic decline, $F_{\rm p}$ rises over the first $\sim$1500 days to a maximum of $\approx$3 mJy before declining rapidly. The offset of epoch 1 suggests that the first radio detection may correspond to a different emission phase or even a distinct emission process. We therefore exclude it from the following analysis.

3.2. Outflow–CNM: Equipartition Analysis

We first consider an outflow–CNM model in which a single impulsive ejecta interacts with the CNM, driving a forward shock that powers the observed synchrotron radio emission. Using the equipartition formalism of R. Barniol Duran et al. (2013), we infer the CNM properties from the measured spectral peak parameters ($\nu_{\rm p}$, $F_{\rm p}$) and the electron index p. The emission is assumed to arise from a thin spherical shell with radius R and thickness $\Delta R = 0.1R$, adopting an area filling factor $f_{\rm A} = 1$ and a volume filling factor $f_{\rm V} \approx 0.36$. Postshock microphysics is parameterized by the dimensionless energy fractions $\epsilon_{\rm e}$ and ϵ_B, defined as the fractions of postshock internal energy deposited into nonthermal electrons and magnetic fields, respectively. We adopt fiducial values $\epsilon_{\rm e} = \epsilon_B = 0.1$ following Y. Cendes et al. (2024). Under these assumptions, the radius of the emitting region is:

$$\begin{aligned} R \approx\ & (1 \times 10^{17}\ {\rm cm}) \times (21.8 \times 525^{p-1})^{\frac{1}{13+2p}} \gamma_{\rm m}^{\frac{2-p}{13+2p}} \\ & \times F_{\rm p,\,mJy}^{\frac{6+p}{13+2p}} d_{\rm L,28}^{\frac{2(p+6)}{13+2p}} \nu_{\rm p,10}^{-1} (1+z)^{-\frac{19+3p}{13+2p}} \\ & \times f_{\rm A}^{-\frac{5+p}{13+2p}} f_{\rm V}^{-\frac{1}{13+2p}} 4^{\frac{1}{13+2p}} \Gamma^{\frac{p+8}{13+2p}} \epsilon^{\frac{1}{17}}, \end{aligned} \quad (2)$$

where $F_{\rm p,\,mJy}$ is the peak flux density in mJy, $d_{\rm L,28}$ is the luminosity distance in units of 10^{28} cm, $\nu_{\rm p,10}$ is the observed peak frequency in units of 10 GHz, z is the redshift, and Γ is the bulk Lorentz factor of the emitter. Following Y. Cendes et al. (2024), deviations from equipartition are captured by $\epsilon = (11/6)\epsilon_B/\epsilon_{\rm e}$, which modifies the radius by a factor of $\epsilon^{1/17}$. We also include the factor of $4^{1/(13+2p)}$ to account for the isotropic electron distribution in the nonrelativistic case. The minimum electron Lorentz factor is $\gamma_{\rm m} = \max[\chi_{\rm e}(\Gamma - 1), 2]$,

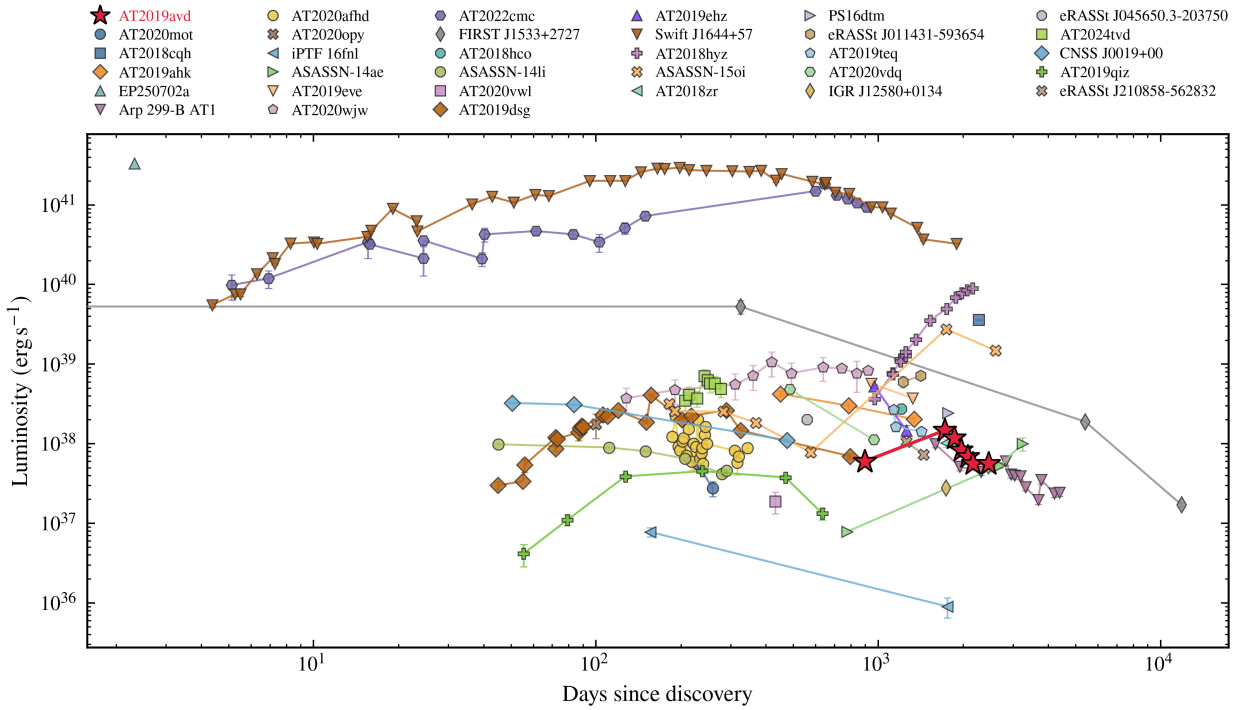

Figure 1. The 5 GHz light curves of radio-detected TDEs selected from the sample of C. Zhou et al. (2026). We retain only measurements obtained within $4.8 \leqslant \nu \leqslant 5.2$ GHz, and define the time offsets relative to the adopted discovery date of each source. The measurements of AT 2019avd are presented in this work. The comparison sources and the references for their radio observations are summarized in Table C1.

where χ_e is defined as

$$\chi_e = \frac{p-2}{p-1}\epsilon_e \frac{m_p}{m_e}, \tag{3}$$

with m_p and m_e denoting the proton and electron masses, respectively.

We then begin with a Newtonian initial estimate by setting $\Gamma = 1$ and $\gamma_m = 2$. A linear fit to $R(t)$ implies an approximately constant expansion velocity of $v = 0.0124 \pm 0.0008c$ and yields an inferred launch time of $t_0 = 58803.5^{+79.6}_{-90.4}$. Given t_0, the shock velocity at each epoch is estimated as

$$v_s = (1+z)\frac{R}{(t_{obs} - t_0)}. \tag{4}$$

At all epochs, $v_s/c \ll 1$, and v_s is consistent with the mean v within 3σ, indicating no significant acceleration or deceleration. We therefore fix $\Gamma = 1$ and $\gamma_m = 2$. With R determined at each epoch, we infer the magnetic-field strength B, the Lorentz factor of electrons radiating at ν_a (γ_a), the number of radiating electrons N_e, the energy in radiating electrons E_e, and the magnetic energy E_B as follows (see Equations (14)–(18) in R. Barniol Duran et al. 2013):

$$\gamma_a \approx 525\, F_{p,\,mJy} d_{L,28}^2 \nu_{p,10}^{-2} (1+z)^{-3} f_A^{-1} R_{17}^{-2} \Gamma, \tag{5}$$

$$N_e \approx (4\times 10^{54}) F_{p,\,mJy}^3 d_{L,28}^6 (1+z)^{-8} \times f_A^{-2} R_{17}^{-4} \nu_{p,10}^{-5} \left(\frac{\gamma_m}{\gamma_a}\right)^{1-p}, \tag{6}$$

$$B \approx 0.013\, F_{p,\,mJy}^{-2} d_{L,28}^{-4} (1+z)^7 \nu_{p,10}^5 f_A^2 R_{17}^4 \Gamma^{-3}\,\mathrm{G}, \tag{7}$$

$$E_e = N_e m_e c^2 \gamma_m \Gamma, \tag{8}$$

$$E_B = \frac{(B\Gamma)^2}{8\pi} V. \tag{9}$$

Here, $V = f_V \pi R^3$ is the volume of the emitting region and $R_{17} \equiv R/10^{17}$ cm. In computing N_e, we included a correction factor of $4(\gamma_m/\gamma_a)^{1-p}$ to account for the isotropic number of radiating electrons in the Newtonian regime and for $\gamma_m < \gamma < \gamma_a$ (see Section 4.2.1 of R. Barniol Duran et al. 2013). The postshock thermal energy is then estimated as $E_s = E_B/\epsilon_B$.The resulting temporal evolution of R, E_s, and B is shown in Figure 4.

Since the thermal energy is approximately equal to postshock kinetic energy, we could derive the ambient densities n_{ext} as:

$$n_{ext} = \frac{M_s}{4Vm_p} = \frac{2E_s}{\left(\frac{3}{4}v_s\right)^2 \times 4Vm_p}, \tag{10}$$

where M_s is the shocked CNM mass, and the factors of 4 and 3/4 account for the compression ratio and postshock velocity under strong-shock conditions (Appendix B in G. Mou 2026). The derived physical parameters are listed in Table B1.

It is worth noting that our analysis adopts a different definition of the minimum energy and a different method for inferring the ambient density compared to some previous studies (e.g., Y. Cendes et al. 2021, 2024). First, we employ the minimum-energy formalism in the *two-component* form (R. Barniol Duran et al. 2013), defined as $E_{eq,2} \equiv E_e + E_B$, which includes only the energy in radiating electrons and magnetic fields. This contrasts with the commonly used *three-component* form, $E_{eq,3} \equiv E_e + E_B + E_p$, which additionally includes the energy of hot protons, $E_p \approx E_e/\epsilon_e$. In most studies, the choice to define $E_p \approx E_e/\epsilon_e$ means that ϵ_e and ϵ_B no longer represent the fractions of postshock thermal energy

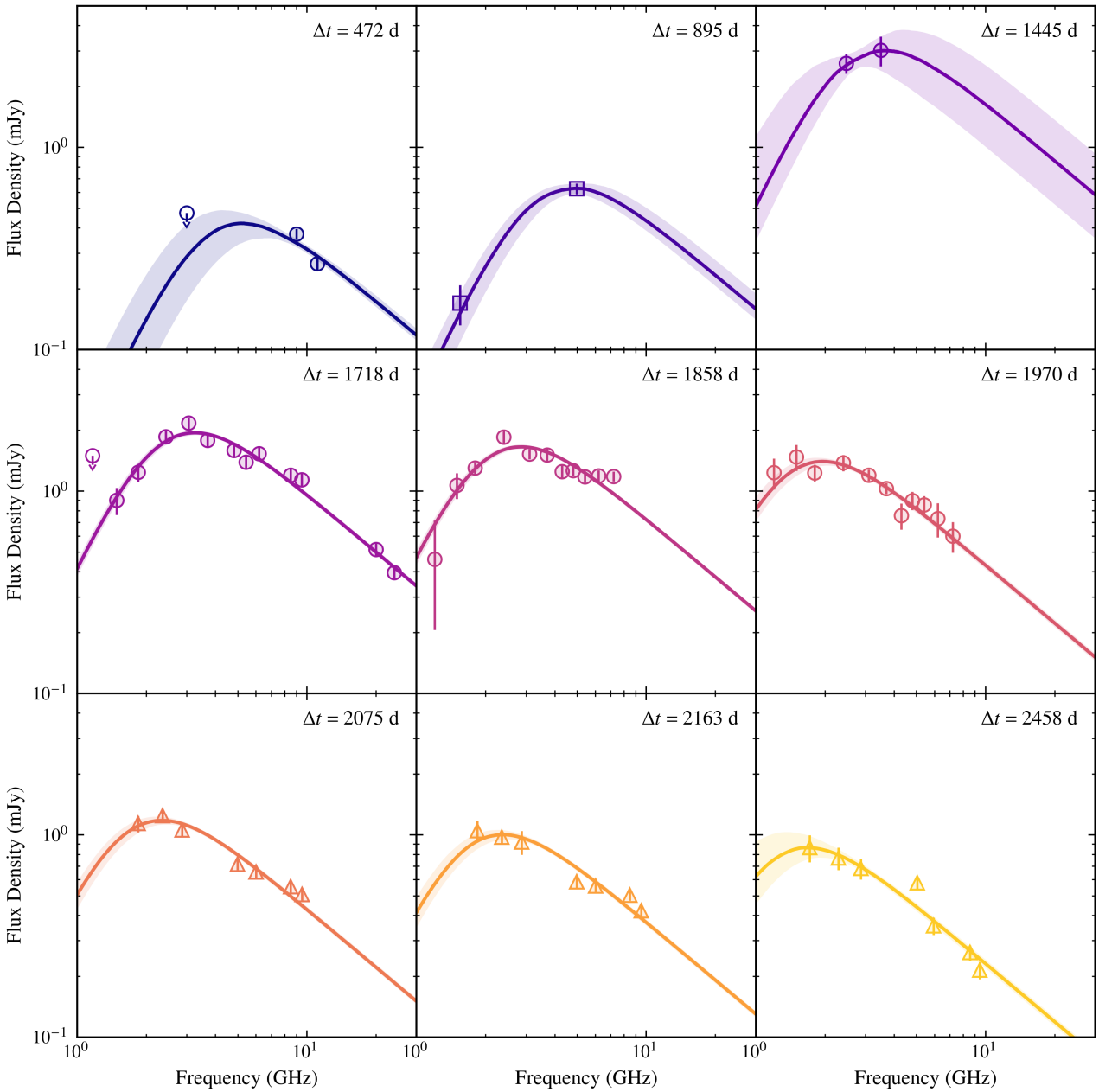

Figure 2. Multiepoch SEDs. Each panel corresponds to a single epoch and is labeled by the time since optical discovery, $\Delta t \equiv t_{\rm obs} - t_{\rm d}$, where $t_{\rm d} = 58523.23$ denotes the time of the optical discovery. Circular, square, and triangular markers denote observations from the VLA, VLBA, and ATCA, respectively, while open symbols with downward arrows represent 3σ upper limits. The solid lines are the best-fit solutions using the phenomenological model from Equation (1), and the shaded regions represent the 1σ confidence intervals of the model fit at each frequency.

carried by electrons and magnetic fields, respectively (see Appendix B in G. Mou 2026 for more details). We therefore adopt the *two-component* form so that $E_{\rm e}$ and $E_{\rm B}$ remain consistent with the chosen $\epsilon_{\rm e}$ and $\epsilon_{\rm B}$.

Second, we infer the CNM density, $n_{\rm ext}$ (Equation (10)), from the kinetic energy of the shocked CNM rather than from the nonthermal electron density, $n_{\rm nte} = N_{\rm e}/(4V)$, which is derived from the number of synchrotron-emitting electrons following a relativistic power-law distribution. The low expansion velocity inferred above, well below the critical value $\beta_{\rm DN} \sim 0.2$ (S. Minhajur Rahaman et al. 2026), indicates that the shocks are in the deep-Newtonian regime. In this regime, only a small fraction of the shocked electrons remain relativistic, such that $n_{\rm nte}$ may underestimate the true ambient density by factors of tens to hundreds (T. Matsumoto & T. Piran 2021). Hereafter, we adopt $n_{\rm ext}$ as the estimate of the CNM density, while $n_{\rm nte}$ is also shown for comparison.

To examine this difference across a broader sample, we selected TDEs from Y. Cendes et al. (2024) with multiepoch constraints on their synchrotron spectral peaks, yielding seven comparison sources, i.e., AT 2018hco (Y. Cendes et al. 2024), AT 2018hyz (Y. Cendes et al. 2022), AT 2019azh (A. J. Goodwin et al. 2022), AT 2019dsg (Y. Cendes et al. 2021), AT 2019eve (Y. Cendes et al. 2024), AT 2020opy (A. J. Goodwin et al. 2023b), and AT 2020vwl (A. J. Goodwin et al. 2023a). We adopted the spectral parameters ($\nu_{\rm p}$, $F_{\rm p}$, p) directly from these

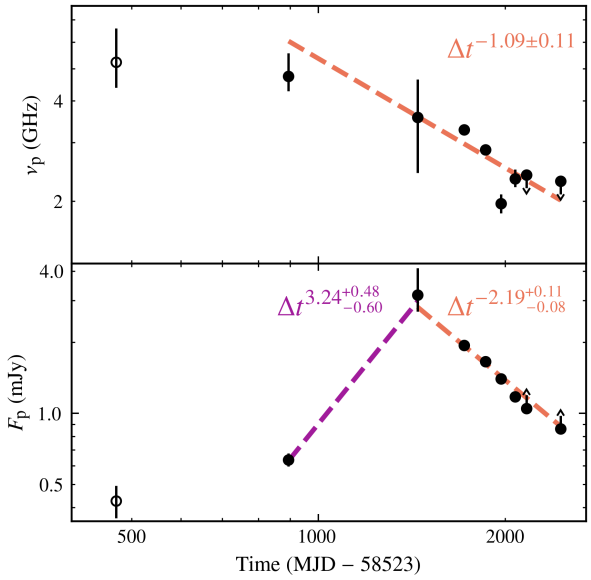

Figure 3. Temporal evolution of the observed peak frequency, ν_p (upper panel), and peak flux density, F_p (lower panel). Dashed lines indicate power-law fits to the data. The open symbol marks epoch 1, which is excluded from the fits. For the last two epochs, the SEDs do not constrain the spectral peak; the arrows show upper limits on ν_p and lower limits on F_p.

studies and recomputed both n_{ext} and n_{nte} using the same equipartition formalism, source geometry, and fiducial microphysical parameters as those adopted for AT 2019avd. The results are shown in Figure 5. Across the comparison sample, n_{ext} is systematically higher than n_{nte}.

3.3. Outflow–cloud

We then considered the outflow–cloud interaction model (G. Mou & W. Wang 2021; G. Mou et al. 2022). In this model, the high-velocity outflow collides with clouds in the vicinity of the SMBH, driving bow shocks on the windward side of the clouds. The radio emission is generated by relativistic electrons accelerated at the bow-shock front. The source exhibits an IR echo lagging the optical flare by several tens of days, indicating the presence of dust clouds at a distance of approximately 0.03 pc from the SMBH (Y. Wang et al. 2023). This provides the necessary conditions for the formation of bow shocks.

We employ the ZEUS3D code (D. A. Clarke 2010) to perform hydrodynamical simulations incorporating relativistic electrons, aiming to investigate whether the radio emission produced by the bow shock can reproduce the observed radio spectrum. The electron acceleration efficiency $\tilde{\epsilon}_e$ is assumed to be the fraction of the energy flux that can be dissipated at the shock (i.e., the change in the kinetic energy flux across the shock) channeled into the relativistic electrons in the downstream. Relativistic electrons are injected into the simulation domain from the shock front grids, with their energy density set to be $e_{cre} = 5/3\tilde{\epsilon}_e e_d$, where e_d is the thermal energy density in the postshock gas (G. Mou & X. Shu 2025), and $\tilde{\epsilon}_e = 0.04$. We assume magnetic fields are dynamically weak and fix a fiducial value of $\epsilon_B = 0.1$. Even so, these fields remain important for relativistic electron cooling and synchrotron emission, and we include them in postprocessing when computing the radio spectra (G. Mou 2026). We modeled the cloud as a toroidal structure orbiting the SMBH, with a

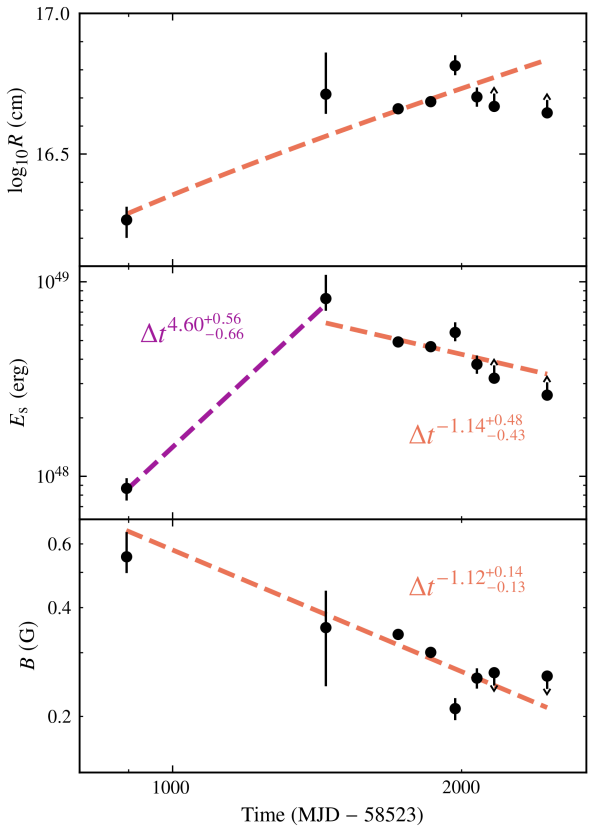

Figure 4. Time evolution of the emitting-region radius R, postshock thermal energy E_s, and magnetic-field strength B inferred from the equipartition analysis. The lower and upper limits are indicated with arrows. In the top panel, the dashed line shows a linear fit of R as a function of $t_{obs} - t_0$, where t_0 is a free parameter representing the outflow launch time. In the other panels, power-law fits are shown for E_s and B as functions of $\Delta t \equiv t_{obs} - t_d$, with $t_d = 58523.23$ denoting the time of optical discovery.

core distance of d_c and a cloud radius of R_c. Given that the IR luminosity of the second flare exceeds that of the first, we speculate that a more powerful outflow was launched during the second outburst. Thus, the onset of the outflow is set to coincide with the second flare at MJD = 59000. The outflow is injected isotropically from the inner boundary of $r_{in} = 3 \times 10^{-3}$ pc into the simulation domain, with the injection sustained for 1 yr, and this duration is basically in line with the second flare's optical plateau stage.

After testing multiple sets of model parameters, we identify a primary set that generally matches the radio observations (Figure 6): $d_c = 0.06$ pc and $R_c = 0.012$ pc. The outflow velocity decreases linearly from $0.1c$ to $0.025c$, and the mass outflow rate is $\dot{M}_{out} = 0.27\ M_\odot\ yr^{-1}$ for the first 30 days, after which it declines overtime linearly from 0.17 to $0.10\ M_\odot\ yr^{-1}$. This setup yields a total outflow mass of $0.145\ M_\odot$ and a cumulative kinetic energy of 6.5×10^{50} erg.

4. Discussion

We analyze more than 5 yr of radio observations of AT 2019avd and derive the physical parameters under both forward-shock and bow-shock scenarios. We discuss possible outflow origins from the outflow–CNM equipartition analysis and the associated tensions in both the outflow–CNM and outflow–cloud scenarios.

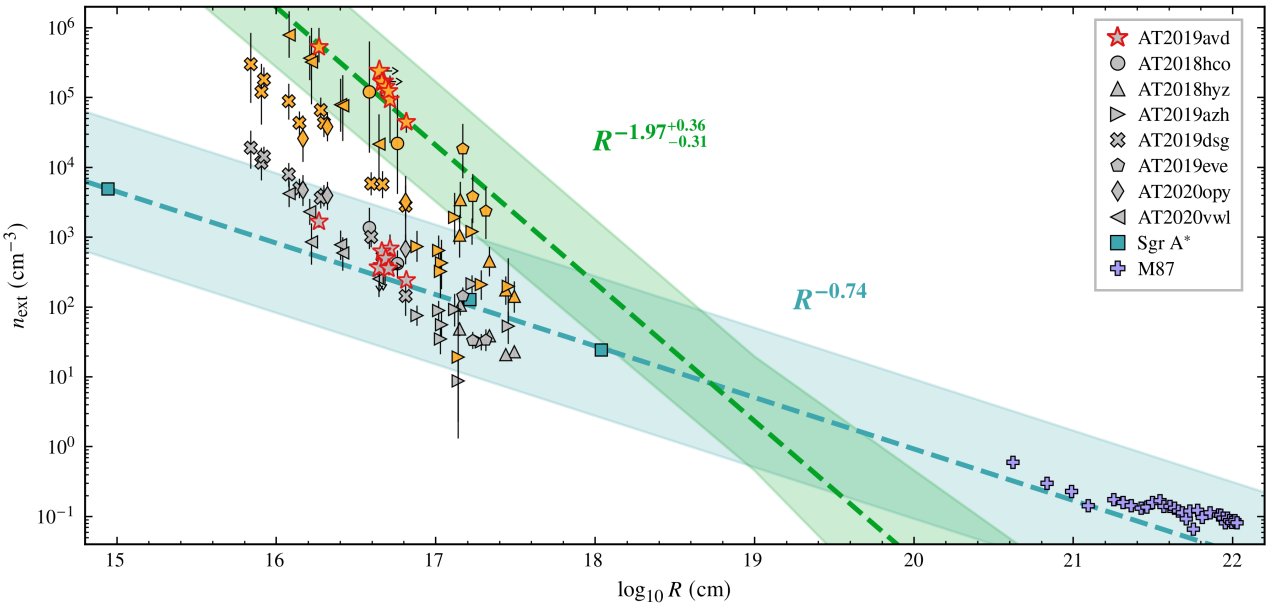

Figure 5. The CNM density profiles of AT 2019avd and the comparison sample of radio TDEs. Yellow markers show ambient densities $n_{\rm ext}$, inferred from the postshock kinetic energy using Equation (10), while gray markers show the nonthermal electron population $n_{\rm nte}$. The green dashed line shows the best-fitting power-law model for the $n_{\rm ext}$ profile of AT 2019avd, with the shaded region indicating the 16th–84th percentile posterior interval. For comparison, the density profiles of Sgr A* (F. K. Baganoff et al. 2003; S. Gillessen et al. 2019) and M87 (H. R. Russell et al. 2015) are also shown. The cyan shaded region denotes ±1 dex around the best-fitting profile of Sgr A*.

4.1. Outflow–CNM Scenario: Outflow Origin

These two well-separated optical flares, with X-ray brightening coincident with the second flare of AT 2019avd have motivated a "two-phase" interpretation, in which the first flare is powered by stream self-intersection (circularization) and the second by delayed accretion through a nascent disk (J.-H. Chen et al. 2022; Y. Wang et al. 2023). Moreover, J.-H. Chen et al. (2022) estimated the onset of the accretion-dominated phase to be MJD 58839^{+3}_{-4} from multiwavelength modeling. Our equipartition analysis yields an outflow launch time of $t_0 = 58803.5^{+79.6}_{-90.4}$, consistent within the uncertainties with the inferred onset of the accretion-dominated phase. Within this context, we discuss the potential physical origins of the observed outflow.

4.1.1. On/Off-axis Relativistic Jets

Both the low outflow velocity ($v \sim 10^{-2}c$) and the subluminous radio emission ($L < 2 \times 10^{38}\,{\rm erg\,s^{-1}}$) of AT 2019avd argue against an on-axis relativistic jet scenario. We further consider the possibility of an off-axis jet using the generalized equipartition formalism for arbitrary viewing angles (T. Matsumoto & T. Piran 2023).

Within this framework, the minimum-energy solutions separate into Newtonian/on-axis and relativistic/off-axis branches, with a continuous connection between the two requiring the apparent Newtonian velocity parameter to exceed a critical value ($\beta_{\rm eq,N} \gtrsim 0.44$; P. Beniamini et al. 2023). For AT 2019avd, we find $\beta_{\rm eq,N} \sim 0.01$ at all epochs, well below this criterion, indicating that an off-axis relativistic solution cannot be smoothly connected to the observed Newtonian evolution. Combined with the observed late-time decline in both peak flux ($F_{\rm p}$) and the postshock thermal energy ($E_{\rm s}$), an off-axis jet would therefore require a rapid deceleration and an abrupt transition to the Newtonian phase between epochs 2 and 3 ($t \sim 1000$–1500 days), for which we find no supporting evidence.

To quantitatively test the off-axis jet scenario, we performed forward modeling with VegasAfterglow (B. Zhang 2018; Y. Wang et al. 2026). We adopted a uniform top-hat jet characterized by an isotropic-equivalent kinetic energy $E_{\rm iso}$, an initial Lorentz factor Γ_0, a half-opening angle $\theta_{\rm c}$, and a viewing angle $\theta_{\rm v}$. The jet propagates into a power-law CNM density profile parameterized by a normalization $A_\star$, and an index, $k_{\rm m}$. The microphysical parameters $\epsilon_{\rm e}$, $\epsilon_{\rm B}$, and $\xi_{\rm e}$, where $\xi_{\rm e}$ denotes the fraction of electrons accelerated into the nonthermal distribution, were assumed to remain constant throughout the modeled period.

We fitted the radio flux-density measurements with `emcee` (D. Foreman-Mackey et al. 2013), considered two possible launch times: $t_0 = 58803.5$, inferred from the equipartition radius evolution, and $t_0' = 59335$, motivated by the onset of the late hard X-ray state reported by Y. Wang et al. (2024). The adopted priors and resulting posterior constraints for both fits are summarized in Table D1.

The models with $t_0 = 58803.5$ and $t_0' = 59335$ yield $\chi^2_\nu = 10.42$ and 5.81, respectively. The later-launch model therefore provides a better fit, although both fits remain statistically unacceptable. As shown in Figure 7. the models systematically overpredict the low-frequency flux densities at $\sim$ 1–2 GHz and fail to reproduce the observed spectral shape around the turnover.

We therefore disfavor the specific off-axis jet model tested here. More complex configurations, including an angularly structured jet, a structured or nonmonotonic CNM, evolving microphysical parameters, or additional low-frequency absorption, may provide a better fit. However, the current data are insufficient to constrain these additional degrees of freedom.

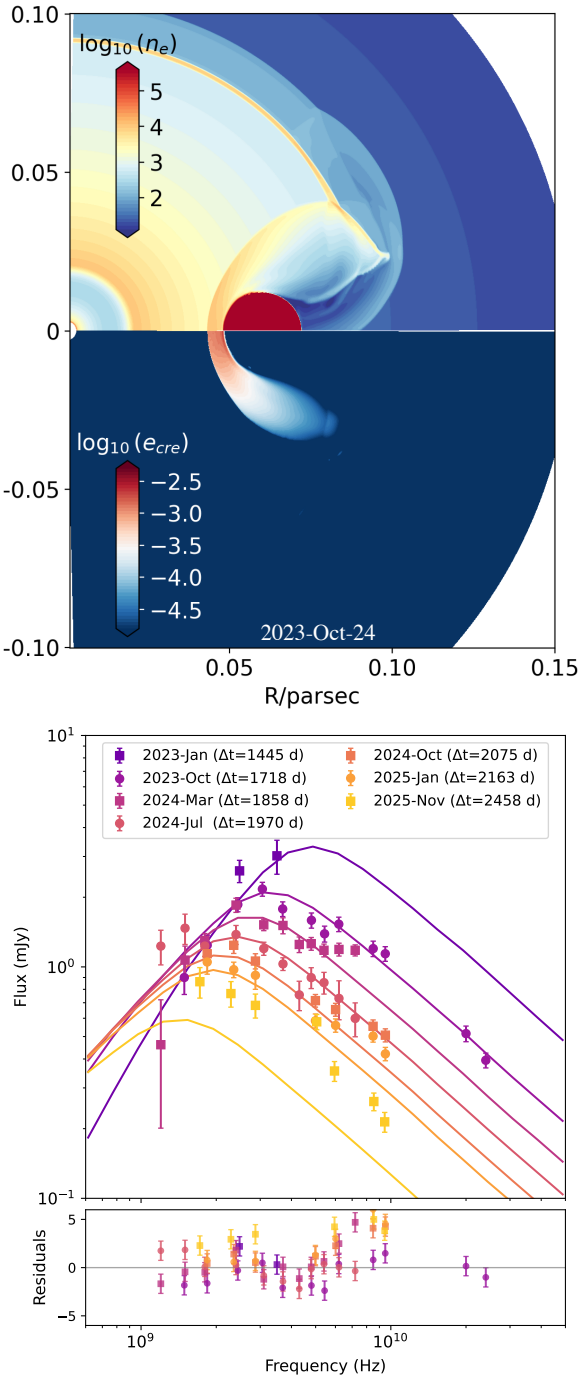

Figure 6. Numerical modeling of the radio emission of AT 2019avd. Upper panel: the thermal gas density n_e (in units of cm^{-3}) and the energy density of relativistic electrons e_{cre} (in units of erg cm^{-3}) for the snapshot of 2023 October 24 ($\Delta t = 1718$ days). Lower panel: comparison between the observed radio spectra and the synthetic spectra at the same epochs. The normalized residuals of (observation-model)/error are shown in the bottom window.

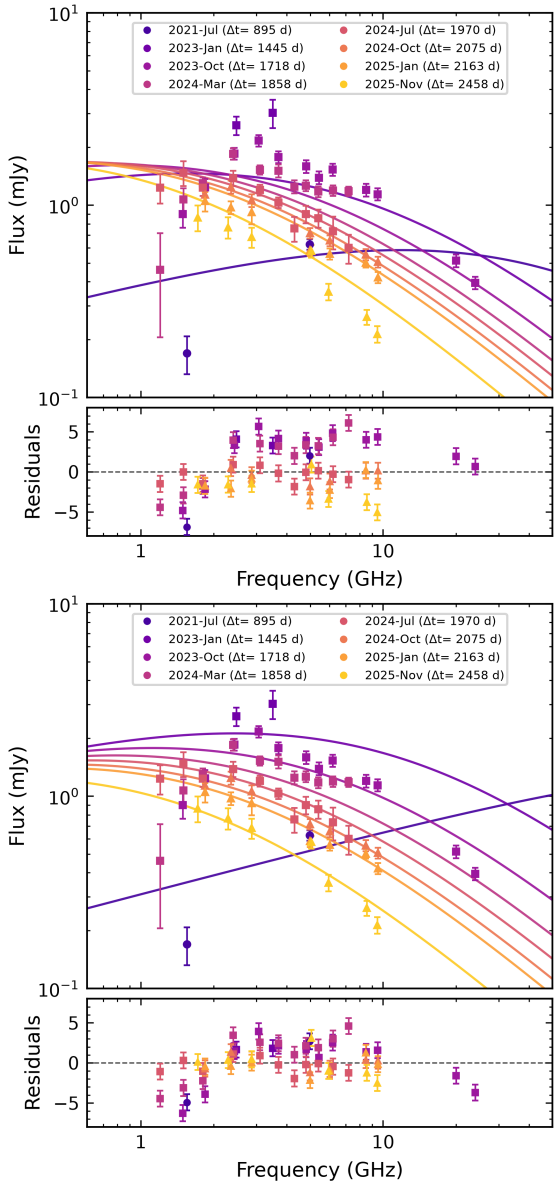

Figure 7. Radio SED fits of AT 2019avd using top-hat jet models computed with `VegasAfterglow`. The upper and lower panels correspond to fixed launch times of $t_0 = 58803.5$ and $t_0' = 59335$, respectively. In each panel, the upper subpanel shows the observed flux densities and the corresponding best-fitting model SEDs, while the lower subpanel shows the residuals, defined as $(F_{\nu,\,\mathrm{obs}} - F_{\nu,\,\mathrm{mod}})/\sigma_{F_{\nu},\,\mathrm{obs}}$.

4.1.2. Unbound Debris

In canonical TDEs, approximately half of the disrupted stellar mass is expected to become unbound and ejected right after the disruption (M. J. Rees 1988).

Simulations show that the maximum speed of the escaping material increases with the penetration factor, R_T/R_p, where R_T and R_p represent the disruption and the pericenter radii, respectively (A. Yalinewich et al. 2019). For a marginal encounter ($R_T/R_p \simeq 1$), the fastest debris reaches $v_{max} \lesssim 0.017c$, whereas even a deeply penetrating disruption ($R_T/R_p \simeq 7$) produces $v_{max} \lesssim 0.07c$. For AT 2019avd, optical light-curve modeling favors a partial disruption with penetration factor $R_T/R_p \simeq 0.56$ (J.-H. Chen et al. 2022), for which the unbound debris is expected to move more slowly and occupy a small solid angle. If we instead adopt a small emitting-area filling factor ($f_A = f_V = 0.008$, based on the $R_T/R_p \simeq 1$ case in A. Yalinewich et al. 2019) in the equipartition analysis, we infer a mean expansion speed is $v = 0.116 \pm 0.007c$, far above expectations for unbound debris. The corresponding launch time, $58803.4^{+79.9}_{-89.7}$, is approximately 280 days after the optical discovery, whereas unbound debris would be produced essentially immediately after the disruption. We therefore disfavor an unbound debris

origin for the outflow responsible for the AT 2019avd radio flare.

4.1.3. CIO or Accretion-driven Outflow

Stream self-intersection is capable of both producing thermal optical/UV emission and driving a quasi-spherical outflow. Subsequently, radio emission is generated as the outflow interacts with the CNM, giving rise to an SSA spectrum whose peak time and luminosity depend on the launch conditions and ambient density (W. Lu & C. Bonnerot 2020). In AT 2019avd, the inferred outflow launch time, t_0, coincides with the onset of the delayed accretion phase. This temporal association therefore disfavors a CIO launched during the initial optical flare as the dominant origin of the radio-emitting outflow.

Simulations predict powerful, wide-angle winds during super-Eddington accretion (L. Dai et al. 2018), and a growing sample of optical TDEs exhibits delayed radio peaks (hundreds to thousands of days) plausibly launched by delayed accretion or accretion state transition (Y. Cendes et al. 2024; K. D. Alexander et al. 2026). In AT 2019avd, the agreement between the inferred outflow launch time, t_0, and the onset of the accretion-dominated phase suggests that the radio-emitting outflow was launched as the accretion flow formed. We therefore identify a delayed, accretion-driven outflow as the most plausible origin of the radio emission in the outflow–CNM interaction scenario.

4.2. Potential Tensions with the Outflow–CNM and Outflow–Cloud Scenarios

4.2.1. The Decrease of the Postshock Energy

The postshock energy exhibits a decline after epoch 3 (middle panel of Figure 4). To assess whether the forward shock has entered the momentum-conserving snowplow phase, we estimate the cooling timescale as follows.

The forward shock velocity of AT 2019avd is estimated to be $\sim 0.01c$, corresponding to a postshock CNM temperature of $T_s = \frac{3}{16}\frac{\mu m_p}{k_B} v_s^2 \approx 1.2 \times 10^8\,\mathrm{K}\left(\frac{v_s}{0.01c}\right)^2$. Given the thermal energy density $e = \frac{3}{2}(n_e + n_i)k_B T_s$, where n_e and n_i are number densities of thermal electrons and ions, the cooling timescale of postshock CNM is $t_{cool} = e/C$. The cooling rate C includes contributions from bremsstrahlung, line cooling, inverse Compton scattering and synchrotron:

$$C = \Lambda n_i n_e + \frac{4}{3} n_e \sigma_T c (u_{rad} + u_{mag})(v_{th}/c)^2, \quad (11)$$

where Λ is the cooling function (R. S. Sutherland & M. A. Dopita 1993), $u_{rad} = L/4\pi R^2 c$ is the radiation energy density, $u_{mag} = B^2/8\pi$, and v_{th} is the thermal velocity. Adopting representative values at $\Delta t \sim 1500$ days, $\Lambda \simeq 3\text{–}6 \times 10^{-23}\,\mathrm{erg\,s^{-1}\,cm^3}$ (for a temperature of 10^{8-9} K), $L < 10^{42}\,\mathrm{erg\,s^{-1}}$, and $B = 0.4$ G, we find that bremsstrahlung dominates the cooling, giving $t_{cool} > 100$ yr.

The long cooling timescale indicates that the forward shock has not yet entered the momentum-conserving snowplow phase, but remains in either the free-expansion phase or the Sedov–Taylor phase, depending on the ejecta mass. In this regime, the postshock energy is expected to increase or remain approximately constant, rather than decline with time.

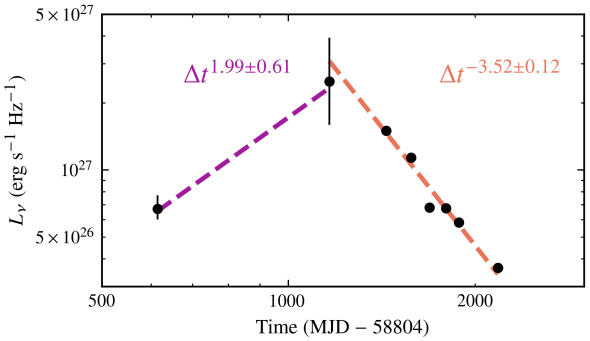

Figure 8. The 9 GHz light curve inferred from the SED model (Section 3.1). The dashed lines show power-law fits to the different temporal phases (two rising segments followed by a decay).

However, the inferred decline assumes time-independent shock microphysics. If ϵ_e decreases with time, the true shock energy could instead remain constant or even increase, a possibility that we cannot completely rule out.

4.2.2. The Rapid Rise and Decline Radio Light Curve

Rapid temporal evolution of the radio luminosity has been proposed as an additional challenge to the outflow–CNM scenario, which predicts a steepest rise of only $L \propto t^3$ (e.g., E. Berger et al. 2012; J. Zhuang et al. 2025). To quantify the radio light-curve evolution of AT 2019avd, we reconstructed the 9 GHz monochromatic luminosity (Figure 8) using the posterior samples from the multiepoch SSA spectral fits (Section 3.1) and modeled its temporal evolution with a broken power law, $L_\nu \propto (t - t_0)^\alpha$, where $t_0 = 58803.5$. The best-fit model yields a rapid rise with $\alpha_r = 1.99 \pm 0.61$, followed by a steep decay with $\alpha_d = -3.52 \pm 0.12$. Within the outflow–CNM framework, G. Mou (2026) derives a relationship between the temporal evolution index, α, and the CNM density profile, k (see their Section 5.3). Adopting $p = 2.91$, we infer $k_r = -0.51 \pm 0.31$ during the rising phase and $k_d = -3.33 \pm 0.06$ during the declining phase of the AT 2019avd light curve. This evolution implies a relatively flat density profile at smaller radii, followed by a much steeper decline at larger radii, opposite to the trend expected in steady-state stellar-wind-fed CNM models, in which the density profile generally flattens toward larger radii (A. Generozov et al. 2017). By contrast, the outflow–cloud interaction scenario naturally predicts both rapid brightening and fading phases (G. Mou & W. Wang 2021; G. Mou & X. Shu 2025), motivating the exploration of this alternative interpretation in Section 3.3.

4.2.3. The Relatively High Density Profile

For comparison with TDEs, we also include the density profile for two of the best-studied galactic nuclei, Sgr A^* and M87, in Figure 5. At the characteristic CNM radii of $R \sim 10^{16-17}$ cm, the comparison TDEs generally exhibit steeper radial density gradients than those inferred for Sgr A^* and M87, while also occupying a substantially higher-density regime. To quantify this difference, we fit the density profiles of AT 2019avd and Sgr A^* with a single power law, $n_{ext} \propto R^k$, obtaining $k = -1.97^{+0.36}_{-0.31}$ for AT 2019avd, and $k \sim -0.74$ for Sgr A^*.

A steep density profile is not unique to AT 2019avd. In our comparison sample, the best-fitting density indices span a broad range, from $k \sim -0.8$ to -4.8, with four sources clustering around $k \sim -2$ to -3. This diversity suggests that steep radial density gradients are relatively common among radio TDEs. However, systematic uncertainties nevertheless remain. Although $n_{\rm ext}$ is a more physically meaningful quantity than $n_{\rm nte}$ in the deep-Newtonian regime, its absolute normalization still depends on the assumed geometry, filling factors, and microphysical parameters. It therefore remains unclear whether the steep CNM profile inferred for TDEs are intrinsic or partly driven by methodological biases.

4.2.4. The Late-time SED Deviation from the Outflow–Cloud Scenario

In the outflow–cloud model, the interaction between the outflow and a toroidal cloud located in the equatorial plane drives a bow shock on the inner (windward) face of the cloud. This shock efficiently accelerates electrons, leading to a substantial population of relativistic particles (Figure 6, see Figure E1 and Figure E2 for the time evolution).

We compute synthetic synchrotron spectra in the polar direction using radiative transfer (see Appendix E of this paper and Section 4 in G. Mou 2026 for more details). The resulting synthetic spectra are generally consistent with the multiepoch radio data, although the discrepancy is largest for the final epoch.

The late-time deviations may arise from an additional contribution of the forward shock, which becomes increasingly important as the mass of the swept-up CNM approaches the ejecta mass. Alternatively, the outflow may have encountered an additional cloud at larger radii that is not included in our simulations, with the associated bow shock contributing extra radio emission. In the former scenario, the radio luminosity may not decline in future observations and could even increase.

We emphasize that the simulation parameters—including those describing the cloud and the outflow—are not uniquely constrained due to limited observational constraints and uncertainties in the microphysics (such as $\epsilon_{\rm e}$ and ϵ_B). Our tests indicate that a cloud radius $R_{\rm c}$ in the range of 0.01–0.02 pc can reproduce the observed spectra. As noted in G. Mou & X. Shu (2025), in the bow-shock scenario the characteristic radius R derived from equipartition effectively traces the cloud size, rather than the forward-shock radius as in the outflow–CNM scenario.

Moreover, our tests show that smaller cloud radii lead to higher opacity, shifting the synchrotron self-absorption peak to higher frequencies. On the other hand, the peak frequency becomes relatively insensitive to further increase in cloud radius beyond a certain scale (Appendix E, Figure E3). Consequently, the upper limit of the cloud size remains uncertain.

5. Conclusion

We presented a detailed study of the radio flare from AT 2019avd spanning more than 5 yr. We modeled each epoch with a synchrotron self-absorbed spectrum and used the inferred spectral parameters to test outflow–CNM and outflow–cloud interaction scenarios. Our main conclusions are as follows:

1. The multiepoch radio spectra are well described by a single SSA component at each epoch. The first radio detection deviates from the later evolution in both $\nu_{\rm p}$ and $F_{\rm p}$, which implies a different origin at early times.
2. In the outflow–CNM framework, our equipartition analysis suggests a nonrelativistic expansion with $v \simeq 0.01c$ and a launch time of MJD $58803.5^{+79.6}_{-90.4}$. The inferred kinematics and energetics disfavor both on-axis and off-axis relativistic jet scenarios, as well as an origin in unbound debris. The launch time instead favors an accretion-driven outflow associated with the delayed accretion phase.
3. The equipartition results reveal several tensions with a simple single-blob outflow–CNM interaction scenario but do not rule out this class of models in general. More complex scenarios involving evolving microphysical properties or a structured CNM remain viable.
4. The outflow–cloud interaction scenario can reproduce most of the observed radio spectra. The presence of the required dense material is supported by the IR brightening coincident with the optical flares. The final epoch exhibits the largest deviation from the bow-shock model, indicating the emergence of an additional component at late times. This component may correspond to a forward shock that becomes increasingly important as the swept-up CNM mass grows or to a second interaction between the outflow and another dense cloud.

Overall, AT 2019avd supports a picture in which bow shocks can dominate the radio flare of some TDE candidates, while a forward shock may contribute increasingly at late times. However, the physical origin of the latest radio spectrum is unclear. Continued radio monitoring, can test the origin of the late-time emission. VLBI imaging may provide constraints on the source size and centroid motion predicted by off-axis jet models. Moreover, a larger sample is required to examine different implementations of the equipartition analysis.

Acknowledgments

We thank the anonymous referee for the constructive comments and suggestions that have improved and reshaped the manuscript. The authors thank the participants of the TDE FORUM (Full-process Orbital to Radiative Unified Modeling) online seminar series for their inspiring discussions. This research was supported by the National Natural Science Foundation of China (NSFC) under grant No. 12588202; by the New Cornerstone Science Foundation through the New Cornerstone Investigator Program and the XPLORER PRIZE; by the Strategic Priority Program of the Chinese Academy of Sciences under grant No. XDB0550203. G.M. was supported by the NSFC (No. 12473013). S.d.P. acknowledges support from ERC Advanced grant 789410.

Software: Python (G. Van Rossum & F. L. Drake 2009), Astropy (Astropy Collaboration et al. 2013, 2018, 2022), NumPy (C. R. Harris et al. 2020), SciPy (P. Virtanen et al. 2020), pandas (W. McKinney 2010; The pandas development team 2020), emcee (D. Foreman-Mackey et al. 2013), dynesty (J. S. Speagle 2020; S. Koposov et al. 2025), bilby (G. Ashton et al. 2019; C. Talbot et al. 2025), Matplotlib (J. D. Hunter 2007), CASA (CASA Team et al. 2022), VegasAfterglow (B. Zhang 2018; Y. Wang et al. 2026), VLASS Scripts (E. Carlson et al. 2022).

Appendix A
Radio Observations

We summarize the radio observations of AT 2019avd in Table A1.

Table A1
Radio Observations of AT 2019avd

Date (UTC)	Instrument	Proposal ID	Frequency (GHz)	Flux Density (mJy)	Error (mJy)
2020-05-25[a]	VLA	20A-514	9.0	0.37	0.02
			11.1	0.27	0.02
2020-08-09[a]	VLA	VLASS 2	3.0	<0.48	⋯
2021-06-22[a]	VLBA	BW142	1.6	0.17	0.04
2021-08-22[a]	VLBA	BW142	5.0	0.63	0.04
2023-01-24	VLA	VLASS 3	2.5	2.60	0.29
			3.5	3.02	0.51
2023-10-10	VLA	23B-301	1.2	<0.90	⋯
			1.5	0.90	0.14
			1.8	1.24	0.13
			2.4	1.86	0.13
			3.1	2.17	0.15
			3.7	1.78	0.13
			4.8	1.59	0.12
			5.4	1.39	0.11
			6.2	1.53	0.11
			8.5	1.20	0.09
			9.5	1.14	0.08
2023-11-07	VLA	23B-301	20.0	0.52	0.04
			24.0	0.40	0.03
2024-03-12	VLA	24A-434	1.2	0.46	0.26
			1.5	1.07	0.16
			1.8	1.30	0.09
			2.4	1.85	0.13
			3.1	1.53	0.09
			3.7	1.51	0.12
			4.3	1.25	0.10
			4.8	1.26	0.08
			5.4	1.18	0.08
			6.2	1.19	0.08
			7.2	1.18	0.07
2024-07-01	VLA	24A-434	1.2	1.23	0.21
			1.5	1.47	0.22
			1.8	1.23	0.12
			2.4	1.38	0.13
			3.1	1.20	0.08
			3.7	1.03	0.07
			4.3	0.76	0.11
			4.8	0.90	0.09
			5.4	0.86	0.09
			6.2	0.73	0.14
			7.2	0.60	0.10
2024-10-12	ATCA	C3662	5.0	0.72	0.05
			6.0	0.65	0.04
			8.5	0.55	0.04
			9.5	0.51	0.03
2024-10-16	ATCA	C3615	1.8	1.14	0.11
			2.4	1.24	0.10
			2.9	1.06	0.08
2025-01-11	ATCA	C3662	1.8	1.05	0.12
			2.4	0.97	0.08
			2.9	0.92	0.12
			5.0	0.59	0.04
			6.0	0.56	0.04
			8.5	0.50	0.03
			9.5	0.42	0.03
2025-10-22	ATCA	C3755	1.7	0.86	0.13
			2.3	0.77	0.10
			2.9	0.68	0.08
2025-11-11	ATCA	C3755	5.1	0.58	0.04
			5.9	0.36	0.04
			8.6	0.26	0.02
			9.4	0.21	0.02

Note. Upper limits are given at the 3σ level. The symbol *a* indicates flux densities taken from Y. Wang et al. (2023).

Appendix B
Spectral Fitting Parameters and Equipartition Analysis Results

We summarize the radio SED fitting results (Section 3.1) and the corresponding equipartition-derived physical parameters (Section 3.2) for each observing epoch in Table B1.

Table B1
Radio SED Parameters and Equipartition Results

Δt (days)	ν_p (GHz)	F_p (mJy)	$\log_{10} R$ (cm)	$\log_{10} N_e$	$\log_{10} B$ (G)	$\log_{10} E_s$ (erg)	$\log_{10} n_{ext}$ (cm^{-3})
895	$4.74^{+0.82}_{-0.46}$	$0.64^{+0.04}_{-0.04}$	$16.27^{+0.05}_{-0.06}$	$52.68^{+0.05}_{-0.06}$	$-0.26^{+0.07}_{-0.05}$	$47.94^{+0.05}_{-0.06}$	$5.72^{+0.28}_{-0.22}$
1445	$3.57^{+1.07}_{-1.13}$	$3.17^{+0.94}_{-0.47}$	$16.71^{+0.15}_{-0.07}$	$53.66^{+0.12}_{-0.06}$	$-0.45^{+0.10}_{-0.16}$	$48.91^{+0.12}_{-0.06}$	$4.97^{+0.35}_{-0.62}$
1718	$3.27^{+0.09}_{-0.11}$	$1.94^{+0.05}_{-0.05}$	$16.66^{+0.02}_{-0.02}$	$53.44^{+0.02}_{-0.02}$	$-0.47^{+0.01}_{-0.01}$	$48.69^{+0.02}_{-0.02}$	$5.22^{+0.08}_{-0.07}$
1858	$2.85^{+0.10}_{-0.08}$	$1.66^{+0.04}_{-0.04}$	$16.69^{+0.02}_{-0.02}$	$53.41^{+0.02}_{-0.02}$	$-0.52^{+0.01}_{-0.02}$	$48.67^{+0.02}_{-0.02}$	$5.16^{+0.08}_{-0.08}$
1970	$1.97^{+0.13}_{-0.13}$	$1.40^{+0.06}_{-0.06}$	$16.81^{+0.04}_{-0.03}$	$53.49^{+0.05}_{-0.05}$	$-0.68^{+0.03}_{-0.03}$	$48.74^{+0.05}_{-0.05}$	$4.65^{+0.14}_{-0.15}$
2075	$2.34^{+0.15}_{-0.13}$	$1.18^{+0.05}_{-0.05}$	$16.70^{+0.03}_{-0.03}$	$53.32^{+0.05}_{-0.05}$	$-0.59^{+0.03}_{-0.03}$	$48.58^{+0.05}_{-0.05}$	$5.09^{+0.13}_{-0.14}$
2163	<2.4	>1.05	>16.67	>53.25	< -0.58	>48.50	<5.23
2458	<2.3	>0.86	>16.65	>53.16	< -0.59	>48.42	<5.38

Note. Quoted uncertainties are 1σ asymmetric errors.

Appendix C
Comparison TDE Sample

Table C1 summarizes the comparison radio TDEs selected from the sample of C. Zhou et al. 2026. We retain only measurements obtained within $4.8 \leqslant \nu \leqslant 5.2$ GHz.

Table C1
Properties and Radio Data References for the 5 GHz Radio TDE Comparison Sample

Source	Redshift	Discovery Time	Radio Data References
FIRST J153350.8+272729	0.03243	1986 Nov 6–Dec 13	V. Ravi et al. (2022)
Arp 299-B AT1	0.010411	2005 Jan 30	S. Mattila et al. 2018
IGR J12580+0134	0.00411	2011 Jan 6	J. A. Irwin et al. 2015 Q. Yuan et al. 2016 E. S. Perlman et al. 2017 E. S. Perlman et al. 2022
Swift J1644+57	0.354	2011 Mar 25	E. Berger et al. 2012 B. A. Zauderer et al. 2013 T. Eftekhari et al. 2018 Y. Cendes et al. 2021
ASASSN-14ae	0.0436	2014 Jan 25	Y. Cendes et al. 2024
ASASSN-14li	0.0206	2014 Nov 22	K. D. Alexander et al. 2016 S. van Velzen et al. 2016 J. S. Bright et al. 2018 A. Anumarlapudi et al. 2024
CNSS J0019+00	0.018	2015 Mar 21	M. M. Anderson et al. 2020
ASASSN-15oi	0.0484	2015 Aug 14	A. Horesh et al. 2021a A. Hajela et al. 2025 A. Anumarlapudi et al. 2024
PS16dtm	0.0804	2016 Aug 12	Y. Cendes et al. 2024
iPTF 16fnl	0.016328	2016 Aug 26	A. Horesh et al. 2021b Y. Cendes et al. 2024
AT 2018zr	0.071	2018 Mar 2	Y. Cendes et al. 2024
AT 2018cqh	0.048	2018 Jun 16	F. Zhang et al. 2024 L. Yang et al. 2025
AT 2018hco	0.088	2018 Sep 18	A. Horesh et al. 2018 Y. Cendes et al. 2024
AT 2018hyz	0.04573	2018 Oct 14	S. Gomez et al. 2020 Y. Cendes et al. 2022 I. Sfaradi et al. 2024 A. Anumarlapudi et al. 2024 Y. Cendes et al. 2024 Y. Cendes et al. 2026
AT 2019ahk	0.0262	2019 Jan 29	C. T. Christy et al. 2024b A. Anumarlapudi et al. 2024
AT 2019dsg	0.0512	2019 Apr 9	R. Stein et al. 2021 G. Cannizzaro et al. 2021 Y. Cendes et al. 2021 P. Mohan et al. 2022 Y. Cendes et al. 2024
AT 2019ehz	0.074	2019 Apr 29	Y. Cendes et al. 2024
AT 2019eve	0.081	2019 May 5	Y. Cendes et al. 2024
AT 2019qiz	0.01513	2019 Sep 18	A. O'Brien et al. 2019a A. O'Brien et al. 2019b A. Anumarlapudi et al. 2024 K. D. Alexander et al. 2026
AT 2019teq	0.0878	2019 Oct 20	Y. Cendes et al. 2024 C. Zhou et al. 2026
AT 2020mot	0.070	2020 Jun 14	I. Liodakis et al. 2023 Y. Cendes et al. 2024

Table C1
(Continued)

Source	Redshift	Discovery Time	Radio Data References
AT 2020opy	0.159	2020 Jul 8	A. J. Goodwin et al. 2023b
eRASSt J045650.3−203750	0.077	2020 Sep 8	Z. Liu et al. 2024
AT 2020vdq	0.045	2020 Oct 4	J. J. Somalwar et al. 2025 C. Zhou et al. 2026
AT 2020vwl	0.0325	2020 Oct 8	A. J. Goodwin et al. 2023a A. J. Goodwin et al. 2025
eRASSt J210858−562832	0.043	2020 Oct 26	A. J. Goodwin et al. 2025
AT 2020wjw	0.1	2020 Nov 28	A. J. Goodwin et al. 2024
eRASSt J011431−593654	0.16	2020 Nov 24	A. J. Goodwin et al. 2025
AT 2022cmc	1.19325	2022 Feb 11	I. Andreoni et al. 2022 D. R. Pasham et al. 2023 L. Rhodes et al. 2023
AT 2020afhd	0.027	2024 Jan 1	Y. Wang et al. 2025 C. T. Christy et al. 2024a
AT 2024tvd	0.04494	2024 Aug 25	I. Sfaradi et al. 2025
EP250702a	1.036	2025 Jul 2	D. Li et al. 2026 A. J. Levan et al. 2025

Appendix D
Off-axis Jet Model

Table D1 lists the prior ranges and posterior constraints for the off-axis jet fits described in Section 4.1.1.

Table D1
Prior and Posterior Constraints for the Off-axis Jet Model Fits

Parameter	Prior Range	Posterior	
t_0	Fixed	58803.5	59335.0
$\log_{10}E_{\rm iso}$	[50, 60]	$56.10^{+0.53}_{-0.55}$	$54.40^{+0.85}_{-0.96}$
$\log_{10}\Gamma_0$	[1, 4]	$3.24^{+0.46}_{-0.58}$	$2.71^{+0.75}_{-0.83}$
$\theta_{\rm c}$	[0.001, 0.5]	0.01 ± 0.01	$0.05^{+0.04}_{-0.01}$
$\theta_{\rm v}$	[0, $\pi/2$]	$0.39^{+0.05}_{-0.04}$	$0.35^{+0.50}_{-0.08}$
$\log_{10}A_\star$	[−2, 2]	$-1.38^{+0.52}_{-0.43}$	$0.31^{+1.31}_{-1.11}$
$k_{\rm m}$	[0.5, 4.0]	0.51 ± 0.01	$1.47^{+0.42}_{-0.22}$
p	[2.01, 4.0]	3.25 ± 0.07	$3.26^{+0.12}_{-0.15}$
$\log_{10}\epsilon_{\rm e}$	[−3, −0.3]	$-1.99^{+0.83}_{-0.66}$	$-1.75^{+0.52}_{-0.76}$
$\log_{10}\epsilon_{\rm B}$	[−6, −0.3]	$-4.85^{+0.98}_{-0.77}$	$-3.63^{+2.36}_{-1.43}$
$\log_{10}\xi_{\rm e}$	[−3, 0]	$-1.66^{+0.63}_{-0.56}$	$-1.84^{+0.52}_{-0.62}$

Appendix E
Numerical Simulations

Through simulations, the resulting distributions of cosmic-ray electron energy density and magnetic field enable modeling of the associated synchrotron emission. Prior to the radiative transfer calculations, we transform the data from the two-dimensional spherical coordinates used in the simulation to a cylindrical coordinate system. This transformation facilitates radiative transfer calculations along the polar direction and allows us to derive the radio spectra.

To improve computational efficiency, we apply this coordinate and grid transformation only to the bow-shock region (i.e., the radiative zone enclosed by the bow shock) using an interpolation method, as illustrated in Figure 2 in G. Mou (2026). The cylindrical grid consists of 64 zones along the vertical (Z) axis and 60 zones in the radial direction.

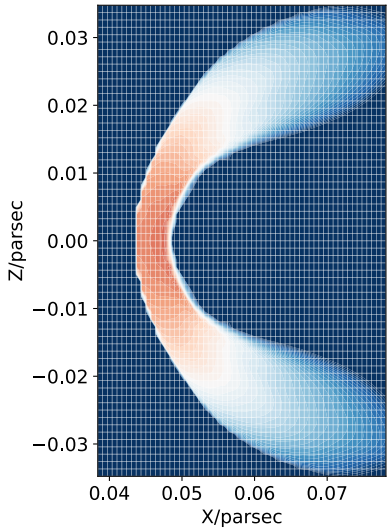

Figure E1. Distribution of e_2 in the cylindrical coordinate system after coordinate and grid transformation.

Figure E1 shows the transformed data for 2023 October 24 ($\Delta t = 1718$ days).

Under the assumption that physical quantities remain constant within an individual grid cell, the variation of the specific intensity I_ν along a ray segment of length Δz is governed by: $\Delta I_\nu/\Delta z = -\alpha_\nu I_\nu + j_\nu$, where j_ν represents the synchrotron volume emissivity and α_ν is the corresponding absorption coefficient.

The formal solution of the radiative transfer equation across a single, homogeneous grid cell yields the specific intensity at the downstream boundary. Denoting this intensity as $I_\nu(i+1)$, it is related to the upstream intensity $I_\nu(i)$ by:

$$I_\nu(i+1) = I_\nu(i)e^{-\Delta\tau_\nu(i)} + S_\nu(i)\left[1 - e^{-\Delta\tau_\nu(i)}\right]. \quad \text{(E1)}$$

Here, $S_\nu(i) = j_\nu(i)/\alpha_\nu(i)$ is the source function in the ith cell, and $\Delta\tau_\nu(i) = \alpha_\nu(i)\Delta x_i$ is the corresponding optical depth. Starting from an initial background intensity at the first cell,

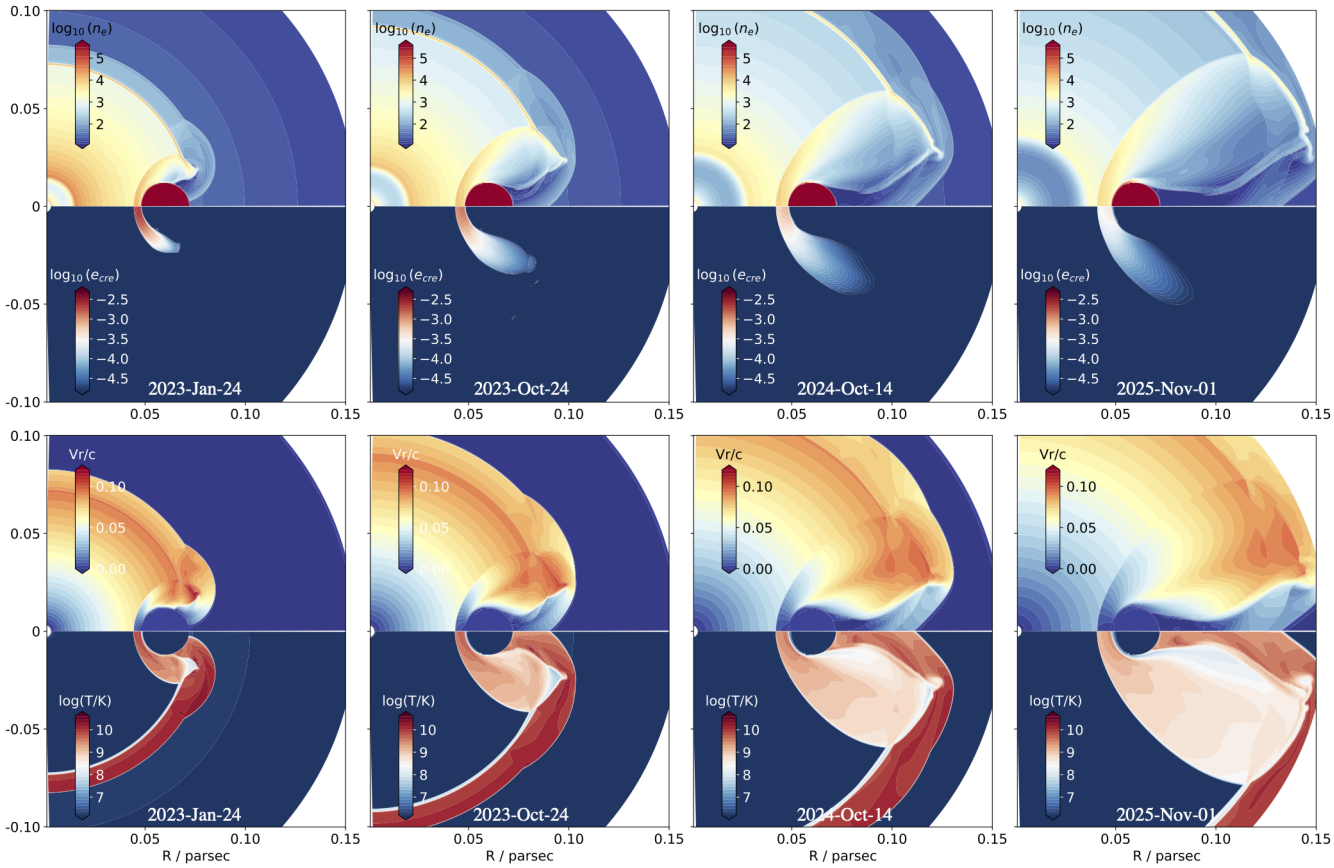

Figure E2. Temporal evolution of outflow–cloud interactions. The upper panels show the density distribution and the energy density of cosmic-ray electrons. The lower panels show the radial velocity (in unit of light speed) and temperature.

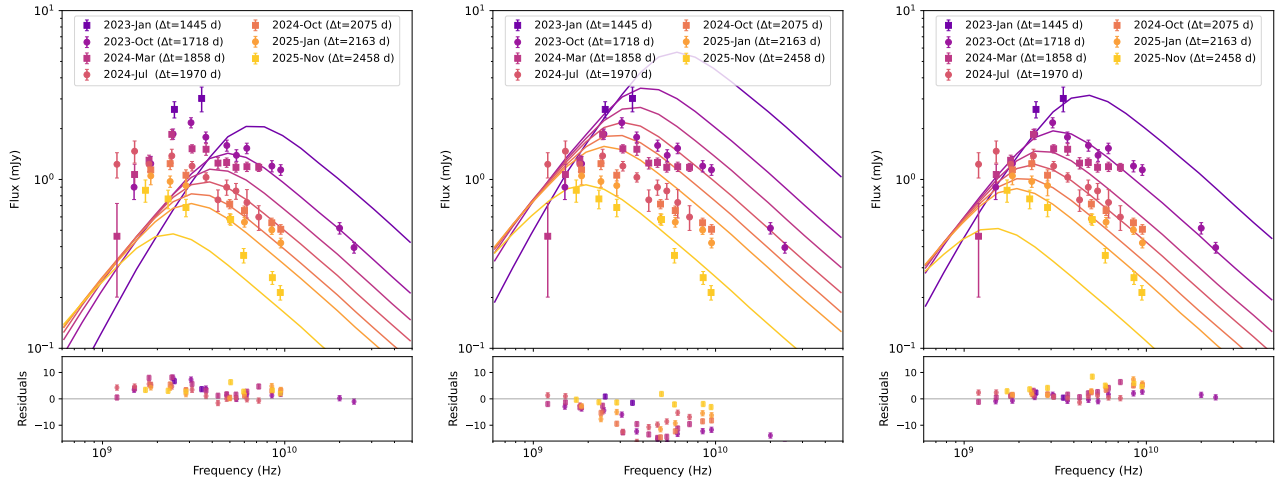

Figure E3. Synthetic radio spectra for models with different cloud distances (d_c) and sizes (R_c). The left panel displays a model in which d_c and outflow velocity are reduced simultaneously ($d_c = 0.036$ pc; velocity decreasing linearly from $0.05c$ to $0.0125c$), while all other parameters remain unchanged ($R_c = 0.012$ pc and $\dot{M}_{\rm out} = 0.17\,M_\odot\ {\rm yr}^{-1}$). The middle panel illustrates the effect of increasing only the cloud size to $R_c = 0.02$ pc (relative to the model presented in the main text with $R_c = 0.012$ pc). The right panel presents a model with $R_c = 0.02$ pc that reproduces the observations by scaling the mass outflow rate to $\dot{M}_{\rm out} = 0.11\,M_\odot\ {\rm yr}^{-1}$ through adjusting the outflow density alone.

this solution is applied iteratively along the entire line of sight to obtain the emergent intensity $I_{\nu,N}$ from the final (Nth) cell at the far boundary of the emitting region.

The total spectral flux density F_ν is then obtained by integrating the emergent intensity $I_{\nu,N}$ over the projected surface of the radiative zone facing the observer: $F_\nu = \int_{\rm surface} I_{\nu,N} \cos\theta\, d\Omega$, where θ is the angle between the local surface normal and the observer's line of sight, and $d\Omega$ is the solid angle subtended by a surface element at the source distance.

For the polar direction, the flux is calculated by summing over cylindrical annuli:

$$F_\nu = \frac{1}{d_L^2}\sum_R I_{\nu,N}(R)\cdot 2\pi R\Delta R, \quad \text{(E2)}$$

where d_L represents the luminosity distance of AT2019avd.

After exploring a range of parameter sets, we selected a representative case that reproduces the observed spectra for presentation in the main text. The temporal evolution of this case is shown in Figure E2. Figure E3 compares the synthetic spectra produced by three distinct models. The spectral analysis indicates that reducing the cloud size leads to a more compact emitting region, which shifts the synchrotron self-absorption peak to higher frequencies. As the cloud size increases, however, the peak frequency becomes relatively insensitive to further changes in cloud size. A larger R_c requires a lower mass outflow rate to recover a similar radio flux. In this case, the increase in the sight-line length of the radiative zone is offset by the simultaneous decline in relativistic electron density and magnetic-field strength, resulting in only a marginal variation in the synchrotron optical depth.

ORCID iDs

Shuyuan Wei https://orcid.org/0009-0005-5669-8465
Yanan Wang https://orcid.org/0000-0003-3207-5237
Guobin Mou https://orcid.org/0000-0002-0092-7944
Linhui Wu https://orcid.org/0000-0003-3454-6522
Santiago del Palacio https://orcid.org/0000-0002-5761-2417
Ranieri D. Baldi https://orcid.org/0000-0002-1824-0411
Xiaolong Yang https://orcid.org/0000-0002-4439-5580
Yang Huang https://orcid.org/0000-0003-3250-2876

References

Alexander, K. D., Berger, E., Guillochon, J., Zauderer, B. A., & Williams, P. K. G. 2016, ApJL, 819, L25
Alexander, K. D., van Velzen, S., Horesh, A., & Zauderer, B. A. 2020, SSRv, 216, 81
Alexander, K. D., Margutti, R., Gomez, S., et al. 2026, ApJ, 1000, 139
Anderson, M. M., Mooley, K. P., Hallinan, G., et al. 2020, ApJ, 903, 116
Andreoni, I., Coughlin, M. W., Perley, D. A., et al. 2022, Natur, 612, 430
Anumarlapudi, A., Dobie, D., Kaplan, D. L., et al. 2024, ApJ, 974, 241
Ashton, G., et al. 2019, ApJS, 241, 27
Astropy Collaboration, Price-Whelan, A. M., Lim, P. L., et al. 2022, ApJ, 935, 167
Astropy Collaboration, Price-Whelan, A. M., Sipőcz, B. M., et al. 2018, AJ, 156, 123
Astropy Collaboration, Robitaille, T. P., Tollerud, E. J., et al. 2013, A&A, 558, A33
Baganoff, F. K., Maeda, Y., Morris, M., et al. 2003, ApJ, 591, 891
Barniol Duran, R., Nakar, E., & Piran, T. 2013, ApJ, 772, 78
Beniamini, P., Piran, T., & Matsumoto, T. 2023, MNRAS, 524, 1386
Berger, E., Zauderer, A., Pooley, G. G., et al. 2012, ApJ, 748, 36
Bloom, J. S., Giannios, D., Metzger, B. D., et al. 2011, Sci, 333, 203
Bright, J. S., Fender, R. P., Motta, S. E., et al. 2018, MNRAS, 475, 4011
Brown, G. C., Levan, A. J., Stanway, E. R., et al. 2015, MNRAS, 452, 4297
Cannizzaro, G., Wevers, T., Jonker, P. G., et al. 2021, MNRAS, 504, 792
Carlson, E., Kimball, A., & Patil, P. 2022, Imaging of the Very Large Array Sky Survey, v1.0, Zenodo, doi: 10.5281/zenodo.7076243
CASA Team, Bean, B., Bhatnagar, S., et al. 2022, PASP, 134, 114501
Cendes, Y., Alexander, K. D., Berger, E., et al. 2021, ApJ, 919, 127
Cendes, Y., Eftekhari, T., Berger, E., & Polisensky, E. 2021, ApJ, 908, 125
Cendes, Y., Berger, E., Alexander, K. D., et al. 2022, ApJ, 938, 28
Cendes, Y., Berger, E., Alexander, K. D., et al. 2024, ApJ, 971, 185
Cendes, Y., Berger, E., Beniamini, P., et al. 2026, ApJ, 998, 111
Cenko, S. B., Krimm, H. A., Horesh, A., et al. 2012, ApJ, 753, 77
Chen, J.-H., Dou, L.-M., & Shen, R.-F. 2022, ApJ, 928, 63
Christy, C. T., Alexander, K. D., Franz, N., et al. 2024a, TNSAN, 56, 1
Christy, C. T., Alexander, K. D., Margutti, R., et al. 2024b, ApJ, 974, 18
Christy, C. T., Alexander, K. D., Laskar, T., et al. 2026, ApJ, 1001, 211
Clarke, D. A. 2010, ApJS, 187, 119
Dai, L., McKinney, J. C., Roth, N., Ramirez-Ruiz, E., & Miller, M. C. 2018, ApJL, 859, L20
Eftekhari, T., Berger, E., Zauderer, B. A., Margutti, R., & Alexander, K. D. 2018, ApJ, 854, 86
Foreman-Mackey, D., Hogg, D. W., Lang, D., & Goodman, J. 2013, PASP, 125, 306
Generozov, A., Mimica, P., Metzger, B. D., et al. 2017, MNRAS, 464, 2481
Gillessen, S., Plewa, P. M., Widmann, F., et al. 2019, ApJ, 871, 126
Gomez, S., Nicholl, M., Short, P., et al. 2020, MNRAS, 497, 1925
Goodwin, A. J., van Velzen, S., Miller-Jones, J. C. A., et al. 2022, MNRAS, 511, 5328
Goodwin, A. J., Alexander, K. D., Miller-Jones, J. C. A., et al. 2023a, MNRAS, 522, 5084
Goodwin, A. J., Miller-Jones, J. C. A., van Velzen, S., et al. 2023b, MNRAS, 518, 847
Goodwin, A. J., Anderson, G. E., Miller-Jones, J. C. A., et al. 2024, MNRAS, 528, 7123
Goodwin, A. J., Burn, M., Anderson, G. E., et al. 2025, ApJS, 278, 36
Goodwin, A. J., Mummery, A., Laskar, T., et al. 2025, ApJ, 981, 122
Granot, J., & Sari, R. 2002, ApJ, 568, 820
Hajela, A., Alexander, K. D., Margutti, R., et al. 2025, ApJ, 983, 29
Harris, C. R., Millman, K. J., van der Walt, S. J., et al. 2020, Natur, 585, 357
Hills, J. G. 1975, Natur, 254, 295
Horesh, A., Cenko, S. B., & Arcavi, I. 2021a, NatAs, 5, 491
Horesh, A., Sfaradi, I., Fender, R., et al. 2021b, ApJL, 920, L5
Horesh, A., Sfaradi, I., Bright, J. S., et al. 2018, ATel, 12271, 1
Hunter, J. D. 2007, CSE, 9, 90
Irwin, J. A., Henriksen, R. N., Krause, M., et al. 2015, ApJ, 809, 172
Jiang, N., Dou, L., Wang, T., et al. 2016, ApJL, 828, L14
Koposov, S., Speagle, J., Barbary, K., et al. 2025, joshspeagle/dynesty, v3.0.0, Zenodo, doi: 10.5281/zenodo.17268284
Krolik, J., Piran, T., Svirski, G., & Cheng, R. M. 2016, ApJ, 827, 127
Lacy, M., Baum, S. A., Chandler, C. J., et al. 2020, PASP, 132, 035001
Levan, A. J., Martin-Carrillo, A., Laskar, T., et al. 2025, ApJL, 990, L28
Li, D., Zhang, W., Yang, J., et al. 2026, SciBu, 71, 538
Liodakis, I., Koljonen, K. I. I., Blinov, D., et al. 2023, Sci, 380, 656
Liu, Z., Ryu, T., Goodwin, A. J., et al. 2024, A&A, 683, L13
Lu, W., & Bonnerot, C. 2020, MNRAS, 492, 686
Lu, W., Kumar, P., & Evans, N. J. 2016, MNRAS, 458, 575
Malyali, A., Rau, A., Merloni, A., et al. 2021, A&A, 647, A9
Matsumoto, T., & Piran, T. 2021, MNRAS, 507, 4196
Matsumoto, T., & Piran, T. 2023, MNRAS, 522, 4565
Mattila, S., Pérez-Torres, M., Efstathiou, A., et al. 2018, Sci, 361, 482
McKinney, W. 2010, in Proc. of the 9th Python in Science Conf., ed. S. van der Walt & J. Millman (SciPy), 56
Minhajur Rahaman, S., Granot, J., & Beniamini, P. 2026, arXiv:2604.23567
Mohan, P., An, T., Zhang, Y., et al. 2022, ApJ, 927, 74
Mou, G. 2026, ApJ, 1006, 70
Mou, G., & Shu, X. 2025, arXiv:2510.25033
Mou, G., Wang, T., Wang, W., & Yang, J. 2022, MNRAS, 510, 3650
Mou, G., & Wang, W. 2021, MNRAS, 507, 1684
Newsome, M., Arcavi, I., Howell, D. A., et al. 2024, ApJ, 977, 258
O'Brien, A., Kaplan, D., Murphy, T., Yu, W., & Zhang, W. 2019a, ATel, 13310, 1
O'Brien, A., Kaplan, D., Murphy, T., Yu, W., & Zhang, W. 2019b, ATel, 13334, 1
Pasham, D. R., & van Velzen, S. 2018, ApJ, 856, 1
Pasham, D. R., Lucchini, M., Laskar, T., et al. 2023, NatAs, 7, 88
Perlman, E. S., Meyer, E. T., Wang, Q. D., et al. 2017, ApJ, 842, 126
Perlman, E. S., Meyer, E. T., Wang, Q. D., et al. 2022, ApJ, 925, 143
Ravi, V., Dykaar, H., Codd, J., et al. 2022, ApJ, 925, 220
Rees, M. J. 1988, Natur, 333, 523
Rhodes, L., Bright, J. S., Fender, R., et al. 2023, MNRAS, 521, 389
Russell, H. R., Fabian, A. C., McNamara, B. R., & Broderick, A. E. 2015, MNRAS, 451, 588
Sfaradi, I., Beniamini, P., Horesh, A., et al. 2024, MNRAS, 527, 7672
Sfaradi, I., Margutti, R., Chornock, R., et al. 2025, ApJL, 992, L18
Somalwar, J. J., Ravi, V., Yao, Y., et al. 2025, ApJ, 985, 175
Speagle, J. S. 2020, MNRAS, 493, 3132
Stein, R., Velzen, S., Kowalski, M., et al. 2021, NatAs, 5, 510
Sutherland, R. S., & Dopita, M. A. 1993, ApJS, 88, 253

Talbot, C., Ashton, G., Hübner, M., et al. 2025, bilby-dev/bilby: v2.7.1, Zenodo, doi: 10.5281/zenodo.17533961
The pandas development team 2020, pandas-dev/pandas: Pandas, v3.0.5, Zenodo, doi: 10.5281/zenodo.3509134
Van Rossum, G., & Drake, F. L. 2009, Python 3 Reference Manual (CreateSpace)
van Velzen, S., Anderson, G. E., Stone, N. C., et al. 2016, Sci, 351, 62
Virtanen, P., Gommers, R., Oliphant, T. E., et al. 2020, NaMet, 17, 261
Wang, Y., Chen, C., & Zhang, B. 2026, JHEAp, 50, 100490
Wang, Y., Baldi, R. D., del Palacio, S., et al. 2023, MNRAS, 520, 2417
Wang, Y., Pasham, D. R., Altamirano, D., et al. 2024, ApJ, 962, 78
Wang, Y., Lin, Z., Wu, L., et al. 2025, SciA, 11, 25.9068
Yalinewich, A., Steinberg, E., Piran, T., & Krolik, J. H. 2019, MNRAS, 487, 4083
Yang, L., Shu, X., Mou, G., et al. 2025, ApJL, 993, L2
Yao, Y., Ravi, V., Gezari, S., et al. 2023, ApJL, 955, L6
Yuan, Q., Wang, Q. D., Lei, W., Gao, H., & Zhang, B. 2016, MNRAS, 461, 3375
Zauderer, B. A., Berger, E., Margutti, R., et al. 2013, ApJ, 767, 152
Zauderer, B. A., Berger, E., Soderberg, A. M., et al. 2011, Natur, 476, 425
Zhang, B. 2018, The Physics of Gamma-Ray Bursts (Cambridge Univ. Press)
Zhang, F., Shu, X., Yang, L., et al. 2024, ApJL, 962, L18
Zhou, C., Lei, W.-H., Lei, X., et al. 2026, arXiv:2603.06056
Zhuang, J., Shen, R.-F., Mou, G., & Lu, W. 2025, ApJ, 979, 109